

X-ray photoemission study of $\text{NiS}_{2-x}\text{Se}_x$ ($x = 0.0 - 1.2$)

S. R. Krishnakumar[†] and D. D. Sarma^{*}

Solid State and Structural Chemistry Unit, Indian Institute of Science, Bangalore 560012, India

Abstract

Electronic structure of $\text{NiS}_{2-x}\text{Se}_x$ system has been investigated for various compositions (x) using x-ray photoemission spectroscopy. An analysis of the core level as well as the valence band spectra of NiS_2 in conjunction with many-body cluster calculations provides a quantitative description of the electronic structure of this compound. With increasing Se content, the on-site Coulomb correlation strength (U) does not change, while the band width W of the system increases, driving the system from a covalent insulating state to a pd -metallic state.

I. INTRODUCTION

Pyrite type disulfides of $3d$ transition metals have been extensively studied as these systems are expected to be well suited for the experimental investigations of electron correlation effects in narrow band electron systems. In the isostructural pyrite series, MS_2 ($M = \text{Fe}, \text{Co}, \text{Ni}, \text{Cu}$ and Zn), the physical properties of the system evolves from the progressive filling of the $3d$ bands of e_g symmetry and exhibit a wide variety of electrical and magnetic properties [1,2]. The ground state metallic or insulating properties of the series appear mostly in agreement with the single particle band theory. Thus, FeS_2 and ZnS_2 are insulators where the e_g band is entirely empty for FeS_2 and totally occupied for ZnS_2 , whereas CoS_2 and CuS_2 with $1/4$ and $3/4$ band fillings are metals, as expected [1,2]. However, NiS_2 , in spite of its half-filled e_g band, is insulating in contrast to results based on band structure calculations and is thought to be driven by electron correlations giving rise to the Mott insulating state [3]. It is found that NiSe_2 , with the same pyrite structure, is completely miscible with NiS_2 in the entire composition range, forming the solid solution $\text{NiS}_{2-x}\text{Se}_x$. NiSe_2 is metallic and thus the ground state of the solid solution changes over from insulating to a metallic one at $x_c \sim 0.43$ [4], without any change in the symmetry of the crystal structure [5] and is believed to be an ideal testing ground for various many-body theories for metal-insulator transitions in strongly correlated narrow band electron systems [3].

At room temperature, NiS_2 is a paramagnetic insulator with a band gap of 0.3 eV, estimated from optical studies [6], while the transport measurements suggest an activation energy of 0.2 eV [3]. It is also found that for a narrow range of composition near x_c , the system undergoes a transition from antiferromagnetic insulator to antiferromagnetic metal with decreasing temperature [7]. The low temperature antiferromagnetic metallic state vanishes around $x = 1.0$, leading to a paramagnetic metallic ground state of the system [7]. NiS_2 crystallizes in the cubic pyrite structure ($P\bar{a}3$ space group) with the lattice parameter, $a = 5.620$ Å [8]. Each Ni atom is coordinated with 6 sulphur atoms in a slightly distorted octahedral environment with the $3d$ level split essentially into a lower lying t_{2g} triplet and

a higher lying e_g doublet. The Ni-S distance in NiS₂ ($d_{Ni-S} \simeq 2.40 \text{ \AA}$) is slightly larger than that in other divalent sulphides of Ni, such as NiS ($d_{Ni-S} \simeq 2.39 \text{ \AA}$) and BaNiS₂ ($d_{Ni-S} \simeq 2.32 \text{ \AA}$). One characteristic feature of the structure of NiS₂ is the presence of very short S-S bonds ($d_{S-S} \simeq 2.06 \text{ \AA}$) compared to that in other sulphides, such as NiS ($d_{S-S} \simeq 3.44 \text{ \AA}$) and BaNiS₂ ($d_{S-S} \simeq 3.14 \text{ \AA}$). This leads to the formation of S₂²⁻ dimers, indicating the presence of strong S-S interactions in the system.

The electronic structure of NiS_{2-x}Se_x has been studied extensively over the years, though mainly using UV-photoemission spectroscopy. However, a recent high-resolution UV photoemission study of this series with $x \leq 0.4$ [9] established that the surface electronic structure of this system behaves very differently compared to that of the bulk. These differences can be clearly observed with the surface sensitive UV photoemission technique, appearing close to the Fermi energy and exhibiting interesting changes in the electronic structure as a function of the temperature. These changes can only be seen within 500 meV of E_F and do not appear to affect even the UV photoemission spectrum in the main valence band region appearing nearly 2 eV below E_F . X-ray photoemission spectroscopy is known to be more bulk sensitive than UV-photoemission spectroscopy; therefore, it is more appropriate to use this technique to study the gross electronic structure of NiS₂ and related compounds and its evolution across the solid solution series. It is also well known that electron-correlation effects are important to describe the electronic structure of these systems while single-particle band theories fail. Different configuration-interaction models including electron correlation effects have been proposed to explain the valence band (VB) [10] and core level spectra [11,12] in the past; however, there has been no consistency between different models used and also between models used for the core level and valence band spectra. In the present study, we investigate the electronic structure of NiS_{2-x}Se_x system using X-ray photoelectron spectroscopic measurements in conjunction with parameterized many body calculations based on a single model Hamiltonian with the same set of parameter values for both core level and valence band spectra. Here, we also study the evolution of the core level and valence band

spectra across the solid solution and discuss their implications.

II. EXPERIMENTAL AND THEORETICAL DETAILS

Samples of $\text{NiS}_{2-x}\text{Se}_x$ with $x = 0.0, 0.4, 0.6, 0.8$ and 1.2 used for the present study were prepared by the standard solid state reaction techniques reported in the literature [13]. X-ray diffraction patterns as well as resistivities of the samples were found to be in agreement with the reported data [1,14]. Spectroscopic measurements were carried out in a combined VSW spectrometer with a base pressure of 2×10^{-10} mbar equipped with a monochromatized Al $K\alpha$ x-ray source with an overall instrumental resolution better than 0.8 eV. All the experiments were performed at 120 K and the sample surface was cleaned *in situ* periodically during the experiments by scraping with an alumina file; the surface cleanliness was monitored by recording the carbon 1s and oxygen 1s core level XP signals. The reproducibility of the spectral features were confirmed in each case. The binding energy was calibrated to the instrument Fermi-level that was determined by recording the Fermi-edge region of a clean silver sample.

Core level and valence band (VB) spectra were calculated for NiS_6 cluster with an octahedral structure, within a parameterized many-body multi-band model including orbital dependent electron-electron (multiplet) interactions; the details of these calculations have been described elsewhere [15–18]. The calculations were performed in the symmetry adapted t_{2g} and e_g basis including the TM 3d and the bonding sulphur 3p orbitals. In the calculation for the valence band spectrum, the S 3p spectral contribution was obtained by the resolution broadening of the S 3p partial DOS obtained from the LMTO band structure calculation [13], while the Ni 3d contribution to the spectrum was evaluated within the cluster model. This is reasonable in view of the negligible correlation effects within the broad band S 3p manifold. Moreover, the S 3p spectral distribution is strongly influenced by the short S-S bonds in the S_2^{2-} dimers, not included in the cluster model. In contrast, such effects are described accurately within the LMTO approach. The calculations were

performed by the Lanczos algorithm and the calculated one-electron removal spectra were appropriately broadened to simulate the experimental spectra. In the Ni $2p$ core level calculation, Doniach-Šunjić line shape function [20] was used for broadening the discrete energy spectrum of the cluster model, in order to represent the asymmetric line shape of core levels and is also consistent with other core levels in the system (*e.g.*, S $2p$ and Se $3d$). In the case of valence band spectral calculations, energy dependent Lorentzian function was used for the lifetime broadening. Other broadening effects arising from the resolution broadening and solid state effects, such as the band structure and phonon broadenings, were taken into account by convoluting the spectra with a Gaussian function. The broadening parameters were found to be consistent with values used earlier for similar systems [15–18].

III. RESULTS & DISCUSSIONS

The S $2p$ core level spectra for the samples studied are shown in the main panel of Fig. 1, as open circles. For NiS₂, the experimental S $2p$ spectrum shows a spin-orbit split doublet as expected and the overlapping solid line shows the simulated spectrum using the usual constrain on the intensity ratio (2:1) between the spin-orbit split partners, $2p_{3/2}$ and $2p_{1/2}$ [21]. However, for $x > 0$, we see two more features in the spectra, indicating the presence of overlapping Se $3p$ levels in the same binding energy range. We have analyzed the experimental spectra for $x > 0$ samples in terms of contribution of two spin-orbit split doublets, simulating the S $2p$ and Se $3p$ states and the resulting fits from least-square-error analysis are shown as the overlapping solid lines in each case, illustrating a very good agreement. In the inset I, we show the individual components of the S $2p$ and Se $3p$, separately for $x = 0.8$. In order to estimate the relative Se/S ratio in the surface region of the samples probed by the photoemission technique, we take the ratio of the intensities of Se $3p$ and S $2p$ for $x = 0.4, 0.6$ and 1.2 and normalize with that obtained for $x = 0.8$, assuming that for $x = 0.8$, the surface composition is the same as dictated by the stoichiometry. Thus obtained ratio $\frac{(Se\ 3p/S\ 2p)_x}{(Se\ 3p/S\ 2p)_{0.8}}$ from the fitting procedure are plotted in inset II as open circles

with error bars. We also plot the expected ratio (solid line) in the same inset as a function of the nominal bulk compositions for all $x > 0$. The plot exhibits a good agreement between the experimental and the expected values. This clearly suggests that the surface composition in this system remains close to that of the bulk without any complication arising from surface non-stoichiometry or segregation.

The Se $3d$ spectra for the entire composition range is shown in the main panel of Fig. 2. The spectral features are broad without any clear indication of the expected spin-orbit split doublet ($3d_{5/2}$ and $3d_{3/2}$) signals. Our analysis of the spectral line shape suggests it to be incompatible with a single type of Se atoms in the system, since the spectral shape could not be simulated by a single set of spin-orbit doublet. It is reasonable to expect the presence of two types of Se atoms in $\text{NiS}_{2-x}\text{Se}_x$. These two types of Se atoms are distinguished by the bonded partner within the dimer unit, since one would in general expect $(\text{Se-Se})^{2-}$, $(\text{Se-S})^{2-}$ as well as $(\text{S-S})^{2-}$ units to be present in samples with $2 > x > 0$ in the $\text{NiS}_{2-x}\text{Se}_x$ series. Raman spectroscopy [22] has been used to identify the presence of bond stretching vibrations of S-S, S-Se and Se-Se molecular units in agreement with this point of view. However, the relative abundance of each of these three types of dimers in any sample of given x is not known so far. Since the nearest neighbor chemical environment of Se in $(\text{Se-Se})^{2-}$ is different from Se in $(\text{Se-S})^{2-}$ dimers, the two types of Se are expected to have different binding energies arising from chemical shifts in the core level spectra. Thus, we attempt to describe the spectra with two distinct Se $3d$ spin-orbit split doublets. In inset I, the two components obtained for $x = 1.2$ along with the experimental data and the resulting fit are shown as an example. The resulting fits to the experimental spectra are shown as solid lines in the main panel of Fig. 2, exhibiting good agreement for all x . The observed chemical shift of about 1.0 eV between the two types of Se sites, was found to be the same in all the samples. It is easy to estimate the expected intensity ratio from these two types of Se sites assuming a random substitution of S atoms by Se in $\text{NiS}_{2-x}\text{Se}_x$; this is given by the statistical ratio, $\frac{I_{\text{Se-Se}}}{I_{\text{Se-S}}} = \frac{x}{4(2-x)}$. In inset II, we plot experimentally and theoretically obtained intensity ratios between Se-Se and Se-S pairs (open circles and solid line respectively) against the respective

Se content (x). We find a remarkable agreement between the two, indicating that the Se substitution is indeed random in these samples.

We now turn to the Ni $2p$ core level spectrum which often manifests distinct spectral signatures arising from various many-body interactions. Ni $2p$ spectrum in NiS₂ (see Fig. 3) consists of spin-orbit split, $2p_{3/2}$ and $2p_{1/2}$ peaks at 853.5 eV and 871 eV binding energies, respectively, with pronounced satellite features around 860 eV and 876 eV, indicating the presence of electron correlations in the system. The satellite intensity relative to the main peak appears considerably more intense in the $2p_{1/2}$ region compared to that in the $2p_{3/2}$ region. In order to determine the inelastic scattering background, we have performed electron energy loss spectroscopy (EELS) on these samples, with the same primary energy as that of the Ni $2p$ core level peak. Using a procedure that have been previously employed [16–18], the inelastic background function obtained for NiS₂ is shown in the inset of Fig. 3, as a dotted line. We find that there is an intense and structured contribution from the background function overlapping the $2p_{1/2}$ satellite region, resulting in the anomalously large satellite intensity in the $2p_{1/2}$ region compared to that in the $2p_{3/2}$ region; this feature in the inelastic scattering spectrum of NiS₂ arises from a plasmon band. It is also seen that at about 857 eV, there is a peak-like structure in the inelastic background; this appears at about the same energy position as that of the strong asymmetry in the line shape of the $2p_{3/2}$ main peak. This structure in the inelastic scattering background could have its origin from the inter-band $p - d$ transitions.

We have calculated Ni $2p$ core level and valence band (VB) spectra of NiS₂ within the same model involving a NiS₆ cluster to obtain quantitative many-body description of the electronic structure. In this calculation for Ni²⁺, the electron-electron interaction parameters, $F_{dd}^2 = 9.79$ eV, $F_{dd}^4 = 6.08$ eV, $F_{pd}^2 = 6.68$ eV, $G_{pd}^1 = 5.07$ eV, and $G_{pd}^3 = 2.88$ eV were used. The calculated Ni $2p$ spectrum with the hopping interaction strength ($pd\sigma$), the charge transfer energy (Δ) and Coulomb interaction strength (U_{dd}) being -1.5 eV, 2.0 eV and 4.0 eV, respectively, is shown in the main figure by a solid line overlapping the experimental spectrum (open circles). The calculated spectrum includes the experimentally

determined inelastic background, shown in the inset. There is evidently a good agreement between the experimental and the calculated spectrum. The calculated discrete spectrum arising from this finite-sized cluster calculation without any broadening is also presented as a stick diagram in the main panel. The present results show that it is necessary to take into account the contributions to the experimental spectrum from the extrinsic loss processes in order to provide a proper quantitative description of the spectrum. The previous estimates of various parameter strengths in NiS₂ obtained from a model that included a “conduction band” in addition to the Ni *3d*-S *3p* basis within the cluster model for the core level calculation [11], are $(pd\sigma) = -1.2$ eV, $\Delta = 2.0$ eV, and $U_{dd} = 5.5$ eV. Thus, the present estimates differ significantly for both $(pd\sigma)$ and U_{dd} , where we have a larger estimate for $(pd\sigma)$ and a smaller value for the U_{dd} . However, the $(pd\sigma)$ values estimated for NiS₂ in the present case is similar to that estimated for other divalent nickel sulphides, for example, $(pd\sigma) = -1.4$ eV for NiS [16] and -1.5 eV for BaNiS₂ [17]. Additionally, as we show later in the text, the present estimates are also consistent with the valence band spectrum. The charge transfer energy, Δ , varies considerably for different sulphides of nickel, with NiS₂ having a Δ of 2 eV compared to 2.5 eV for NiS and 1.0 eV for BaNiS₂ [17]. In general, Δ is expected to be smaller for sulphides compared to oxides, since the O *2p* levels are energetically more stable than the S *3p* levels; for example, the estimated Δ for NiO is 5.5 eV [15]. The value of U_{dd} in NiS₂ is found to be the same as that in NiS [16], while in the case of BaNiS₂, U_{dd} estimated is still smaller (~ 3 eV) [17], possibly arising from a more efficient screening in the metallic system due to a smaller Δ and slightly large $(pd\sigma)$ values.

The ground state wavefunction of NiS₂ corresponding to the estimated parameter strengths have been analyzed in terms of contributions from various electron configurations. The ground state of the system was found to consist of 61.6%, 35.1% and 3.3% of d^8 , $d^9\underline{L}^1$, and $d^{10}\underline{L}^2$ configurations with a high-spin configuration ($S = 1$). The average value of the *d*-occupancy (n_d) is found to be 8.42, showing a highly covalent ground state of the system, which is very similar to that obtained for NiS (8.43) [16] and BaNiS₂ (8.48) [17]. We have analyzed the characters of the final states of the system responsible for the

different features in the experimental spectrum in order to understand their origins. The analysis was carried out for some of the representative final state energies marked 1-10 in Fig. 3. The different contributions to the final states from various electron configurations (d^8 , $d^9\underline{L}^1$, $d^{10}\underline{L}^2$) are listed in Table. I. These features can be grouped into three different regions; the main peak region, 852-856 eV (labelled 1-4); intense satellite region, 859-862 eV (labelled 5-8), and weak satellites in the region of 864-867 eV (labelled 9 and 10). The first group of features in the main peak region has a dominant $d^9\underline{L}^1$ character as seen from the table, which are the ‘well-screened’ states of the system, corresponding to one ligand (sulphur) electron being transferred to the Ni site to screen the attractive potential of the Ni $2p$ core-hole created by the photoemission process. This is similar to the observations from previous studies in the charge transfer systems, where $d^9\underline{L}^1$ states are stabilized compared to the other configurations giving rise to the intense main peak. The second group of features have a mixed character with significant contributions from all the configurations. This is in contrast to the case of NiO where the intense satellite structure results primarily from the d^8 configuration, establishing that the satellite in the Ni $2p$ core spectrum in NiS₂ cannot be described as a ‘poorly screened’ state. Such heavily mixed characters of the satellites have been shown to exist for intermetallic compounds of Th [23]. For the third group of features, the primary contribution comes from both d^8 and $d^9\underline{L}^1$ contributions with relatively lower contributions coming from $d^{10}\underline{L}^2$ character.

In Fig. 4, we show the experimental XP valence band spectrum (open circles) along with the calculated spectrum (solid line) using the same model. As mentioned before, we have used the S $3p$ partial DOS obtained from the band structure calculation to represent the S $3p$ contribution to the valence band spectrum. It was also found necessary to shift rigidly the S $3p$ partial DOS by about 0.9 eV to higher binding energy in order to match the experimentally observed S $3p$ features. The various contributions to the calculated spectrum, Ni $3d$ (dashed line) and S $3p$ (dot-dash line) are shown along with the experimental data in Fig. 4. An inelastic scattering background function (dotted lines) is also included in the total calculated spectrum. The calculated discrete contributions from the Ni $3d$ to the

total spectrum for NiS₂ are also shown without any broadening effects as a stick diagram in Fig. 4. The parameter set used for the valence band calculation is identical to that used for the core level calculation. In view of the fact that no parameter was adjusted to obtain a fit, the agreement between the experimental spectrum and the calculated one is remarkable over the entire energy range. The increasing intensity in the experimental spectrum beyond 11 eV is due to S 3s level with a peak at about 14 eV. There are two distinct sets of parameters proposed earlier on the basis of valence band analysis. Fujimori *et al.* [10] obtained $\Delta = 1.8$ eV, $U_{dd} = 3.3$ eV and $(pd\sigma) = -1.5$ eV, while Sangaletti *et al.* [12] arrived at $\Delta = 3.0$ eV, $U_{dd} = 4.5$ eV and $(pd\sigma) = -1.35$ eV. Good agreement between the experimental spectrum and the calculated one in the present study (see Fig. 4) over the entire range with a minimum number of parameters, indicates the reliability of the parameter set estimated here. This is further enhanced by the fact that the same set of parameters also provides an equally satisfactory description of the core level spectrum (see Fig. 3). We note that previous estimates in ref. [10] is in better agreement with the present results, with the ref. [12] arriving at a too high an estimate for Δ and too low an estimate for $(pd\sigma)$.

The main peak region in the valence band spectrum at about 2.3 eV arises essentially from Ni 3d photoemission contribution though there is a small contribution arising from S 3p states also due to hybridization mixing of Ni 3d and S 3p states. The features at 3.5 eV and 7.5 eV are contributed primarily by the S 3p contributions. As the same model and same parameters were used for the VB calculation of NiS₂, the ground state of the system was the same as that described in the core level calculation. The results of the character analysis of the final states labelled 1-11 in Fig. 4 are shown in Table. II. The spectral features can be grouped into three regions, the main peak region (0-3.5 eV, labelled 1-4), the spectral features in the 5-7 eV range (labelled 5-7) and satellites beyond 8.5 eV (marked 8-11). The final states in the main peak region predominantly consist of $d^8\bar{L}^1$ states with non-negligible contributions from $d^9\bar{L}^2$ and d^7 configurations. This is similar to the case of other charge-transfer systems, like NiO [15]. In the 5-7 eV spectral region, the final states have

very similar character as that in the main peak region, with the contributions from $d^8 \underline{L}^1$ further enhanced at the expense of contributions from d^7 and $d^{10} \underline{L}^3$ states. The satellite features at higher energies (marked 8-11) are dominated by d^7 and $d^9 \underline{L}^2$ configurations with little contributions from other configurations. As these satellite features have dominant d^7 character, these could be attributed to the spectral signature of the lower Hubbard band in the system. However, these features are not distinct in the experimental spectrum due to their weak intensities.

We now turn to the results obtained from the solid solution $\text{NiS}_{2-x}\text{Se}_x$ in order to address the changing electronic structure observed with increasing x in the series. The Ni $2p$ core level spectra for the entire series are shown in the main panel of Fig. 5. For all the compositions the spectra appear to be quite similar, though there are some subtle differences between the spectra with different Se contents. The spectra for $x = 0, 0.6$ and 1.2 are overlapped in the inset of Fig. 5 for the $2p_{3/2}$ region. As the Se content increases, the $2p_{3/2}$ level narrows, consistent with the previous report [24]. In this comparison, the satellite intensity relative to the main peak intensity appears to decrease marginally as x increases. This apparent decrease of the satellite intensity is essentially compensated by the narrowing of the main peak, such that the integrated satellite intensity relative to the main peak integrated intensity remains essentially the same. From the core level analysis, we see that the intensity of the satellite peak is sensitive to the value of U . Hence, on the basis of the insensitivity of the satellite intensity, we conclude that all electronic interaction strengths, and in particular the on-site coulomb interaction strength U , do not change significantly across the composition range studied; the same calculated result, as shown in Fig. 3, can explain the different core level spectra in Fig. 5 equally well with slight adjustments of the broadening functions.

The XP valence band spectra of $\text{NiS}_{2-x}\text{Se}_x$ for $x = 0.0, 0.6, 0.8$ and 1.2 recorded using Al $K\alpha$ are shown in Fig. 6. As x increases, the various features marked (A, B, and C) become more evident in the XP spectra; additionally, the separation between the features A and B

increases across the series. As x increases, the Se $4p$ contribution to the VB increases and the changes in feature C can be attributed to this. As the features A and B are dominated by Ni $3d$ states, the spectral changes suggest some subtle modifications in the electronic structure, which is presumably also responsible for the change in the ground state properties with x , namely the insulator-metal transition. However, such effects cannot be treated within the minimal cluster model considered here and more sophisticated approaches like Dynamical Mean Field Theory (DMFT) [25,26] are required to study the detailed electronic structure near E_F . Within the resolution limit of XPS, we do not see any dramatic changes in the valence band spectrum near E_F , across the series. Even for the bulk insulating NiS₂, there is a finite intensity at E_F and this could be due to the resolution broadening, but also might have some contribution coming from the surface metallic layer [9]. However, there is an indication of an increased intensity at E_F with increasing x , consistent with the increase in the metallicity of the solid solution. The metal-insulator transition in NiS_{2-x}Se_x series is an issue which have been studied extensively, however, still not understood completely. Our study reveals that the on-site Coulomb interaction in the system does not change with the increase in the Se substitution. This is consistent with the suggestion of NiS₂ and NiSe₂ having similar U [13]. Moreover, band structure studies [13] reveal that the effective Ni d band width (W) increases in going from NiS₂ to NiSe₂. Thus, as a result of the increase in W , the effective correlation strength (U/W) decreases, driving the system metallic for x above x_c . The estimated values of ($pd\sigma$), Δ and U (-1.5 eV, 2.0 eV and 4.0 eV, respectively), places NiS₂ in the regime of covalent insulators, [27] close to pd -metals. As Se is substituted in place of S, the system moves in to the pd -metallic regime, driven by the decrease in (U/W), resulting in the bulk metal-insulator transition in the system.

In conclusion, we have investigated the electronic structure of NiS_{2-x}Se_x system using x-ray photoemission spectroscopy. The analysis of the S $2p$ and Se $3d$ spectra revealed the homogeneity of the samples, without any segregation or non-stoichiometry. The electronic structure of NiS₂ has been studied by means of a parameterized multi-band cluster model and is found to be successful in describing the core level and valence band spectra within the

same model and an identical parameter set. These calculations show that NiS₂ is a strongly correlated system with a highly covalent character. It is found that the on-site Coulomb interaction strength (U) does not change with the Se substitution and the system transforms from the covalent insulator regime to a *pd*-metallic type, due to the enhanced bandwidth resulting from the substitution of S by Se.

IV. ACKNOWLEDGMENTS

The authors thank the Department of Science and Technology, and the Board of Research in Nuclear Sciences, Government of India, for financial support. SRK thanks the Council of Scientific and Industrial Research, Government of India, and The Abdus Salam International Centre for Theoretical Physics (ICTP), Trieste, Italy for financial assistances. The authors also thank Professor S. Ramasesha and the Supercomputer Education and Research Center, Indian Institute of Science, for providing the computational facility.

REFERENCES

* Also at Jawaharlal Nehru Center for Advanced Scientific Research, Bangalore and Centre for Condensed Matter Theory, Indian Institute of Science, Bangalore.

Electronic address: sarma@sscu.iisc.ernet.in

† Presently at The Abdus Salam International Centre for Theoretical Physics (ICTP), Trieste, Italy.

- [1] J. A. Wilson, in *The metallic and Nonmetallic states of Matter*, P. P. Edwards and C. N. R. Rao, Eds. Taylor and Francis, London, pp. 215-260, (1985).
- [2] J. A. Wilson and A. D. Yoffe, *Adv. Phys.* **18**, 303 (1969).
- [3] J. M. Honig and J. Spalek, *Chem. Mater.* **10**, 2910 (1998).
- [4] S. Sudo, *J. Magn. Magn. Mater.* **57-69**, 114 (1992).
- [5] S. Endo, T. Mitsui and T. Miyadai, *Phys. Lett.* **46A**, 29 (1973).
- [6] R. L. Kautz, M. S. Dresselhaus, D. Adler and A. Linz, *Phys. Rev. B* **6**, 2078 (1972).
- [7] X. Yao, J. M. Honig, T. Hogan, C. Kannewurf and J. Spalek, *Phys. Rev. B* **54**, 17469 (1996).
- [8] T. Fujii, K. Tanaka, F. Marumo and Y. Noda, *Mineral. J. Japan* **13**, 448 (1987).
- [9] D. D. Sarma, S. R. Krishnakumar, E. Weschke, C. Schüßler-Langeheine, C. Mazumdar, L. Kilian, G. Kaindl, K. Mamiya, S.-I. Fujimori, A. Fujimori and T. Miyadai, To appear in *Phys. Rev. B* May 15th issue (2003).
- [10] A. Fujimori, K. Mamiya, T. Mizokawa, T. Miyadai, T. Sekiguchi, H. Takahashi, N. Môri and S. Suga, *Phys. Rev. B.* **54**, 16329 (1996).
- [11] A. E. Bocquet, K. Mamiya, T. Mizokawa, A. Fujimori, T. Miyadai, H. Takahashi, N.

- Môri and S Suga, *J. Phys.: Condens. Matter* **8**, 2389 (1996).
- [12] L. Sangaletti, F. Parmigiani, T. Thio and J. W. Bennett, *Phys. Rev. B* **55**, 9514 (1997).
- [13] D. D. Sarma, M. Pedio, M. Capozzi, A. Girycki, N. Chandrasekharan, N. Shanthi, S. R. Krishnakumar, C. Ottaviani, C. Quaresima and P. Perfetti, *Phys. Rev. B* **57**, 6984 (1998).
- [14] T. Miyadai, M. Saitoh and Y. Tazuke, *J. Magn. Magn. Mater.* **104-107**, 1953 (1992).
- [15] K. Maiti, P. Mahadevan, and D. D. Sarma, *Phys. Rev. B* **59**, 12457 (1999).
- [16] S. R. Krishnakumar, N. Shanthi, Priya Mahadevan and D. D. Sarma, *Phys. Rev. B* **61**, 16370 (2000); S. R. Krishnakumar, N. Shanthi, Priya Mahadevan, and D. D. Sarma, *Phys. Rev. B* **62**, 10570 (2000).
- [17] S. R. Krishnakumar, T. Saha-Dasgupta, N. Shanthi, Priya Mahadevan, and D. D. Sarma, *Phys. Rev. B* **63**, 045111 (2001).
- [18] S. R. Krishnakumar, N. Shanthi, and D. D. Sarma, *Phys. Rev. B* **66**, 115105 (2002).
- [19] Carl J. Ballhausen, *Introduction to Ligand Field Theory*, McGraw-Hill, New York, 1962.
- [20] S. Doniach and M. Šunjić, *J. Phys. C* **3**, 285 (1970).
- [21] J. Nanda, Beena Annie Kuruville and D. D. Sarma, *Phys. Rev. B* **59**, 7473 (1999).
- [22] Th. Stingl, B. Müller and H. D. Lutz, *J. Alloys Compd.* **184**, 275 (1992); V. Lemos, G. M. Gualberto, J. B. Salzberg and F. Cerderia, *Phys. Stat. Sol. (b)* **100**, 755 (1980).
- [23] D. D. Sarma, F. U. Hillebrecht, O. Gunnarsson and K. Schönhammer, *Z. Phys. B* **63**, 305 (1986); O. Gunnarsson, K. Schönhammer, D. D. Sarma, F. U. Hillebrecht and M. Campagna, *Phys. Rev. B* **32**, 5499 (1985).
- [24] W. Folkerts, G. A. Sawatzky, C. Haas, R. A. de Groot and F. U. Hillebrecht, *J. Phys.: Solid State Phys.* **20**, 4135 (1987).

- [25] A. Y. Matsuura, H. Watanabe, C. Kim, S. Doniach, Z.-X. Shen, T. Thio and J. W. Bennett, Phys. Rev. B **58**, 3690 (1998).
- [26] H. Watanabe and S. Doniach, Phys. Rev. B **57**, 3829 (1998).
- [27] D. D. Sarma, H. R. Krishnamurthy, S. Nimkar, S. Ramasesha, P. P. Mitra, and T. V. Ramakrishnan, Pramana - J. Phys. **38**, L531 (1992); S. Nimkar, D. D. Sarma, H. R. Krishnamurthy, and S. Ramasesha, Phys. Rev. B **48**, 7355 (1993).

V. FIGURE CAPTIONS

Fig. 1. S $2p$ core level spectral region for the series $\text{NiS}_{2-x}\text{Se}_x$. For $x > 0$, Se $3p$ contribution in the same spectral region is observed. The solid lines show the result of the analysis of the spectral shape in terms of contributions from S $2p$ and Se $3p$ levels. Individual S $2p$ and Se $3p$ components are shown for $x = 0.8$ in inset I. The Se/S ratio with respect to $x = 0.8$ obtained from the analysis is plotted in inset II as a function of the nominal Se content of the samples.

Fig. 2. Se $3d$ core level spectra for the series $\text{NiS}_{2-x}\text{Se}_x$. The solid lines show the result of the analysis of the spectral shape in terms of contributions from two chemically-distinct Se $3d$ components arising from Se-Se and Se-S pairs. The spectral analysis is illustrated for $x = 1.2$ in inset I in terms of the Se $3d$ components. The intensity ratio between different components (Se-Se and Se-S bonds) obtained from the analysis is shown in inset II as open circles while the solid line represents theoretically expected ratio.

Fig. 3. Experimental Ni $2p$ core level spectrum of NiS_2 (solid circles) along with the inelastic scattering background function (dotted line) obtained from EELS is shown in the inset. Experimental Ni $2p$ spectrum (open circles) along with the calculated spectrum (solid line) for NiS_2 obtained from the cluster calculation is shown in the main panel. Various final states of the cluster calculation and the corresponding intensity contributions without any broadening are shown as the bar diagram.

Fig. 4. The experimental VB spectrum (open circles) along with the calculated spectrum (solid line), Ni $3d$ component (dashed line), S $3p$ component (dot-dashed line) and the integral background (dotted line) are shown for NiS_2 . The final states of the calculation and the corresponding intensities without any broadening are shown as the bar diagram.

Fig. 5. Ni $2p$ core level spectra from the series $\text{NiS}_{2-x}\text{Se}_x$ for various x values are shown in the main panel. Inset shows the Ni $2p_{3/2}$ region for $x = 0, 0.6$ and 1.2 .

Fig. 6. Valence band spectra obtained using Al $K\alpha$ radiation for $\text{NiS}_{2-x}\text{Se}_x$. Various spectral features are marked A, B and C and their evolution across the series is discussed in

the text.

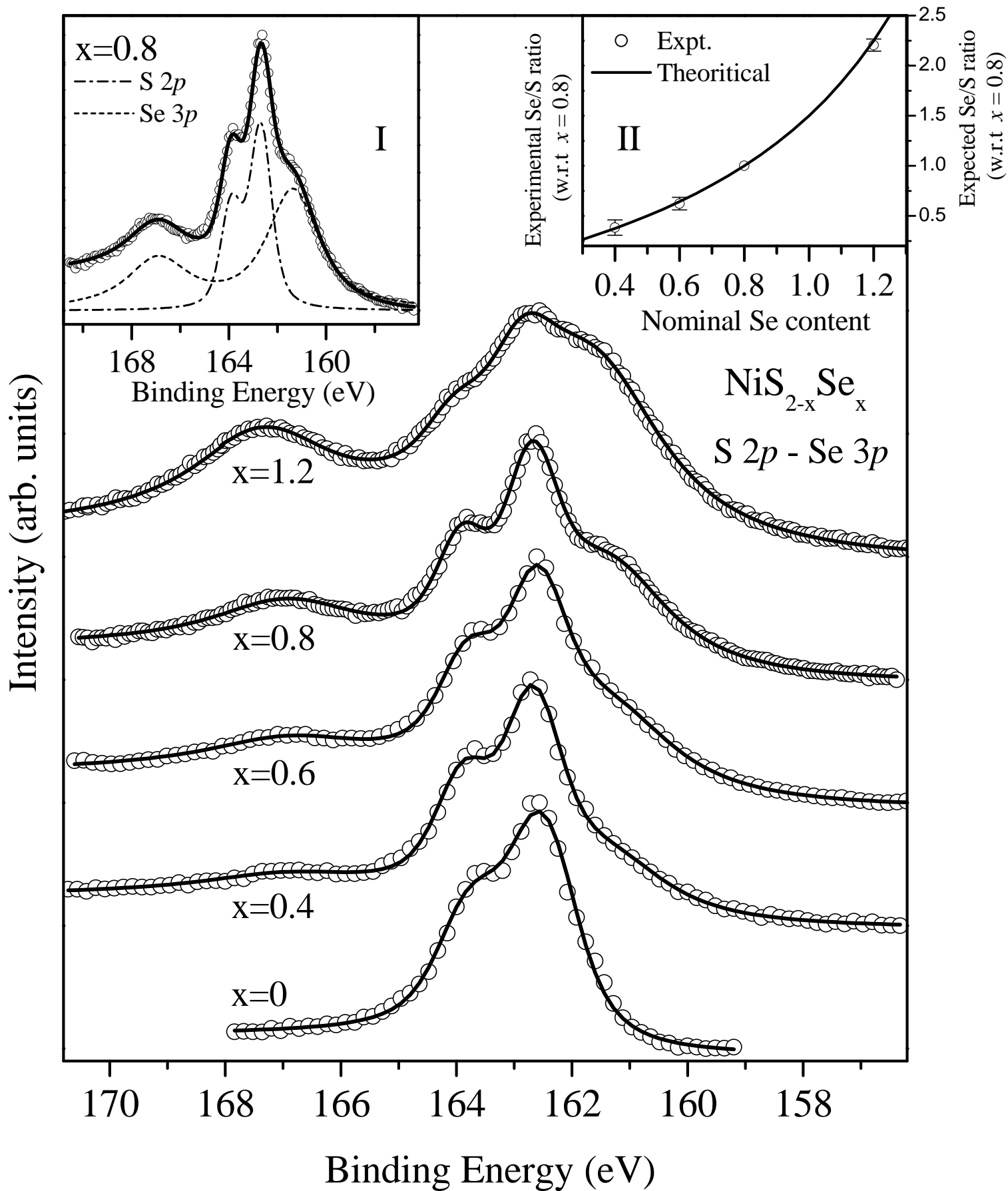
TABLES

TABLE I. Contributions from various configurations in the final states of the Ni $2p$ core level photoemission in NiS₂.

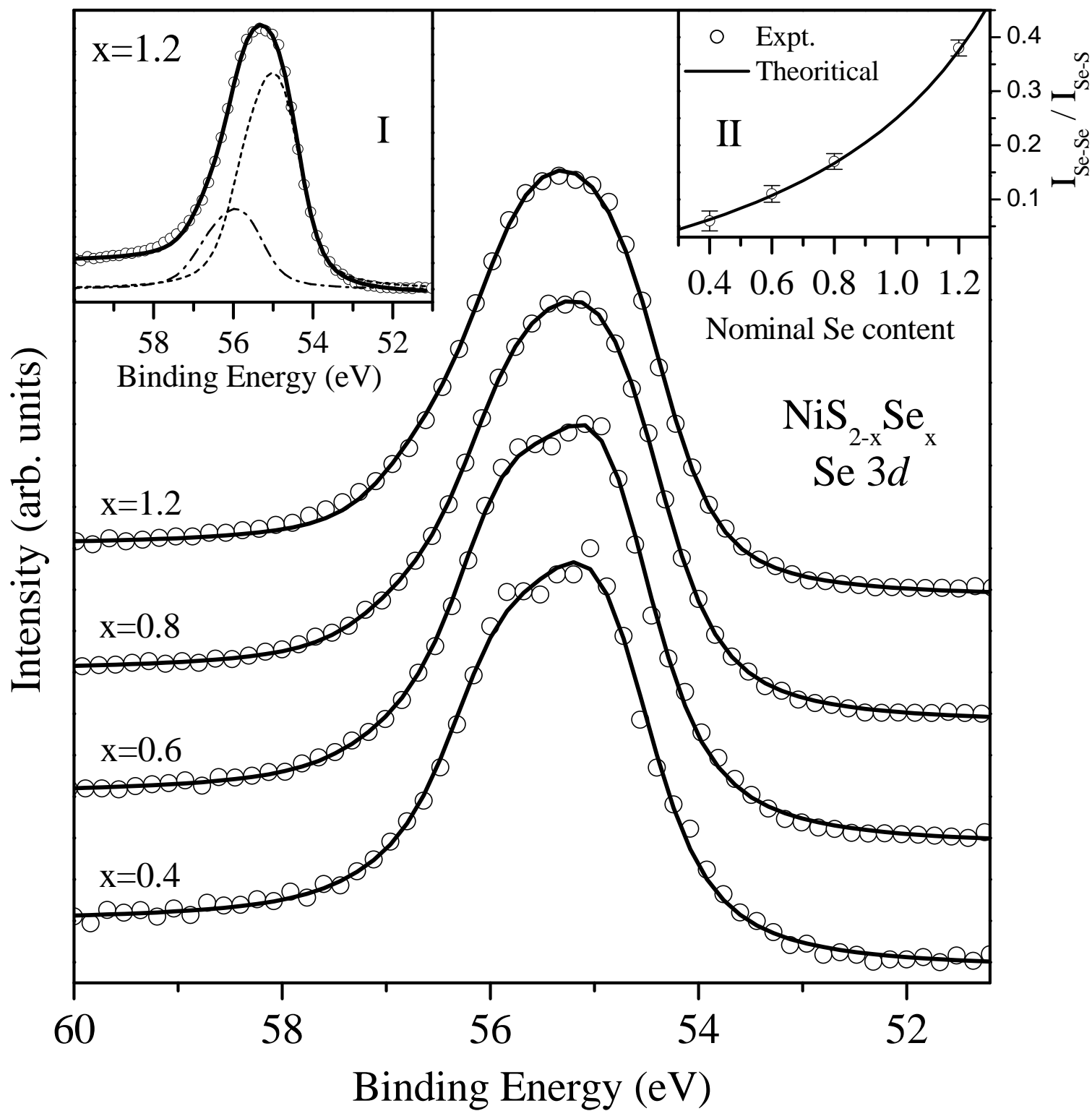
| Peak no. | 1 | 2 | 3 | 4 | 5 | 6 | 7 | 8 | 9 | 10 |
|--------------------------|-------|-------|-------|-------|-------|-------|-------|-------|-------|-------|
| BE | 853.6 | 854.3 | 854.9 | 855.6 | 859.5 | 860.2 | 861.4 | 861.8 | 864.5 | 866.6 |
| d^8 | 26.63 | 16.16 | 21.24 | 9.51 | 40.92 | 37.49 | 34.40 | 21.66 | 35.03 | 58.34 |
| $d^9 \underline{L}^1$ | 56.49 | 61.47 | 60.41 | 63.89 | 29.06 | 25.33 | 12.88 | 23.09 | 41.15 | 32.45 |
| $d^{10} \underline{L}^2$ | 16.88 | 22.37 | 18.35 | 26.60 | 30.02 | 37.18 | 52.72 | 55.25 | 23.82 | 9.21 |

TABLE II. Contributions from various configurations in the final states of valence-band photoemission in NiS₂.

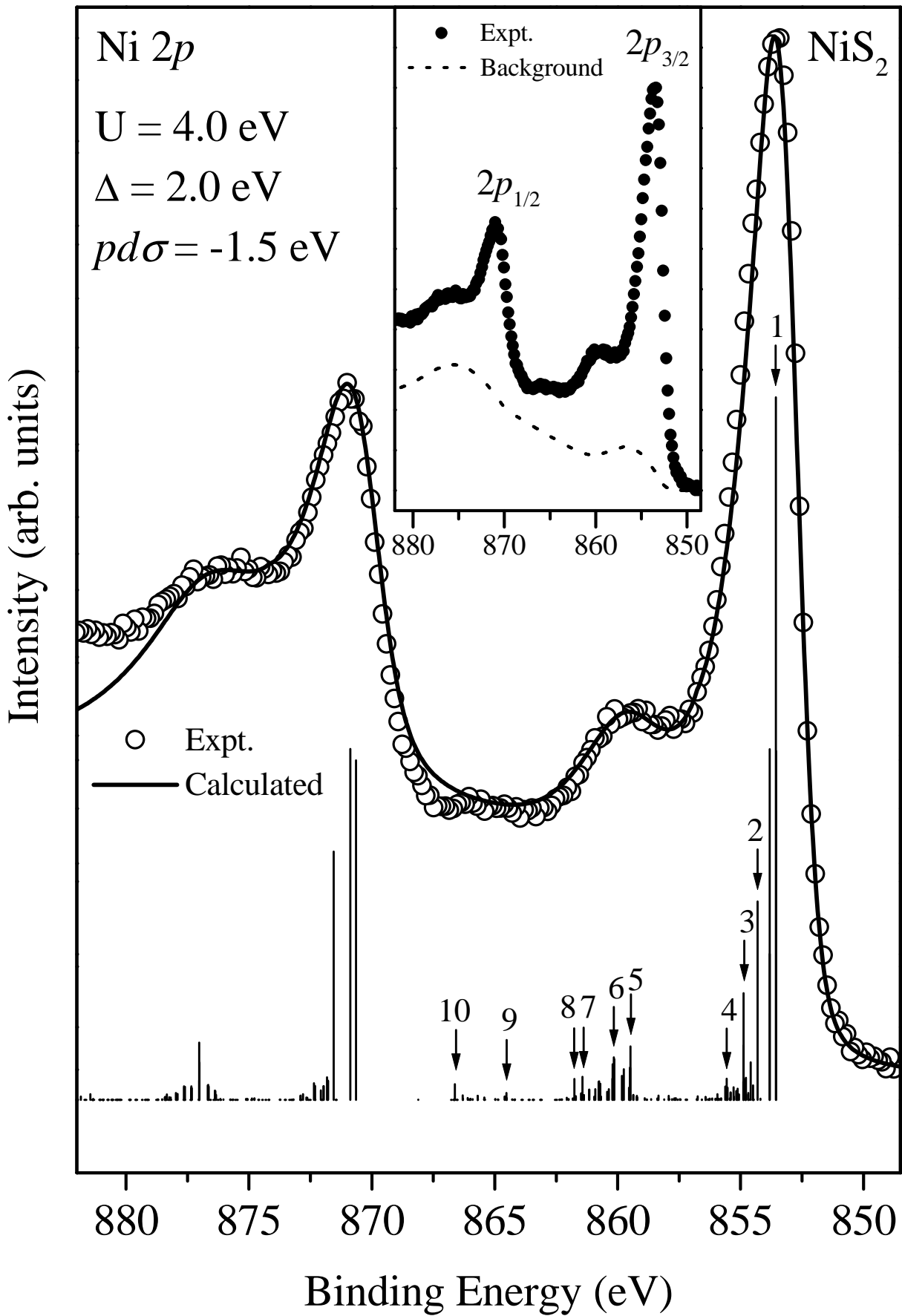
| Peak no. | 1 | 2 | 3 | 4 | 5 | 6 | 7 | 8 | 9 | 10 | 11 |
|--------------------------|-------|-------|-------|-------|-------|-------|-------|-------|-------|-------|-------|
| BE | 2.1 | 2.3 | 3.0 | 3.3 | 5.4 | 5.9 | 6.7 | 8.7 | 9.1 | 9.7 | 10.0 |
| d^7 | 14.50 | 23.86 | 14.75 | 13.71 | 3.44 | 0.00 | 0.38 | 49.33 | 35.43 | 30.06 | 44.72 |
| $d^8 \underline{L}^1$ | 54.53 | 54.34 | 56.63 | 56.13 | 68.17 | 76.32 | 67.05 | 7.15 | 11.32 | 11.06 | 4.65 |
| $d^9 \underline{L}^2$ | 28.26 | 20.38 | 26.52 | 27.92 | 27.24 | 23.68 | 32.12 | 37.25 | 42.77 | 52.17 | 41.59 |
| $d^{10} \underline{L}^3$ | 2.71 | 1.42 | 2.10 | 2.24 | 1.15 | 0.00 | 0.45 | 6.27 | 10.48 | 6.71 | 9.04 |



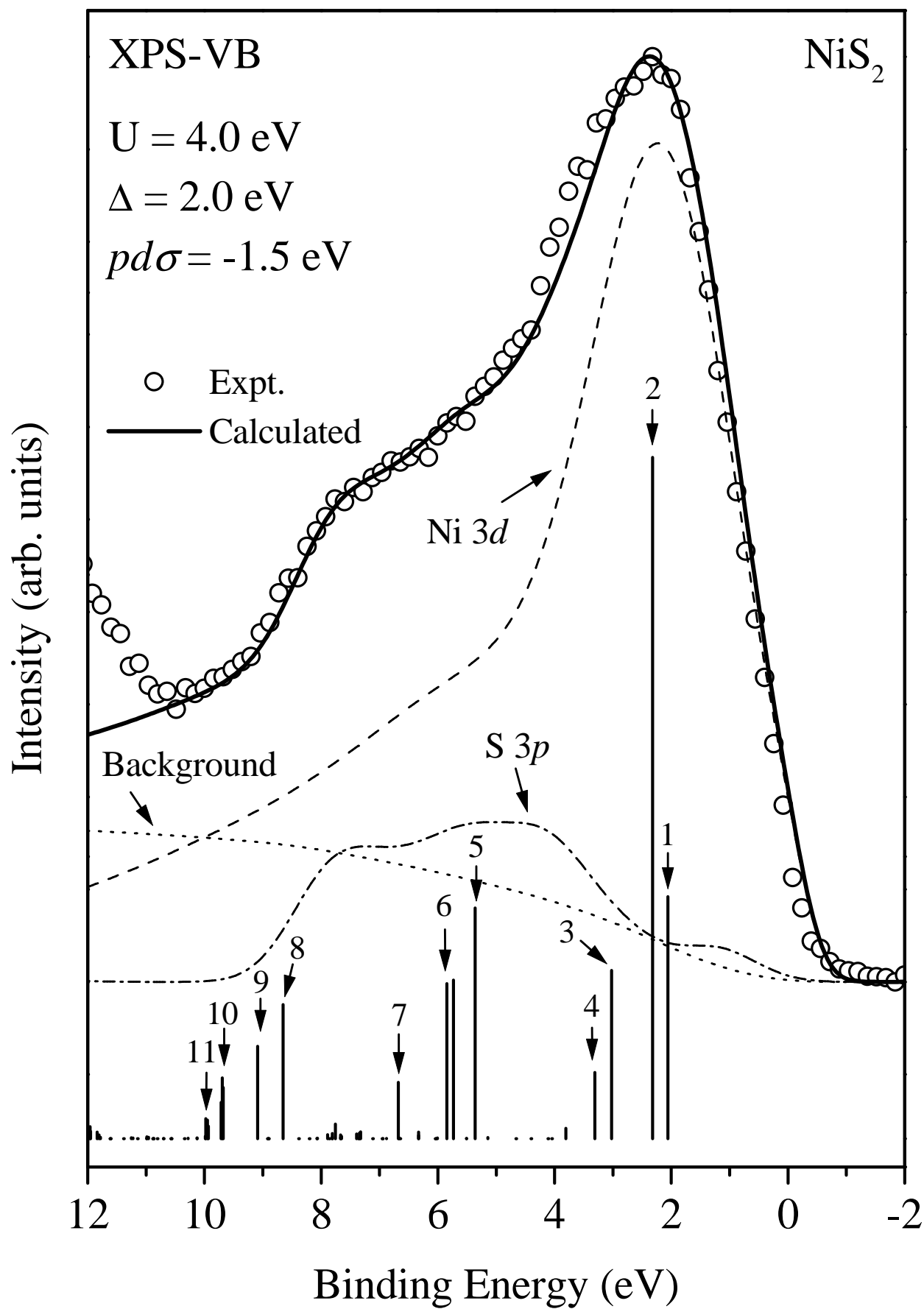
Krishnakumar *et al.*, Fig. 1



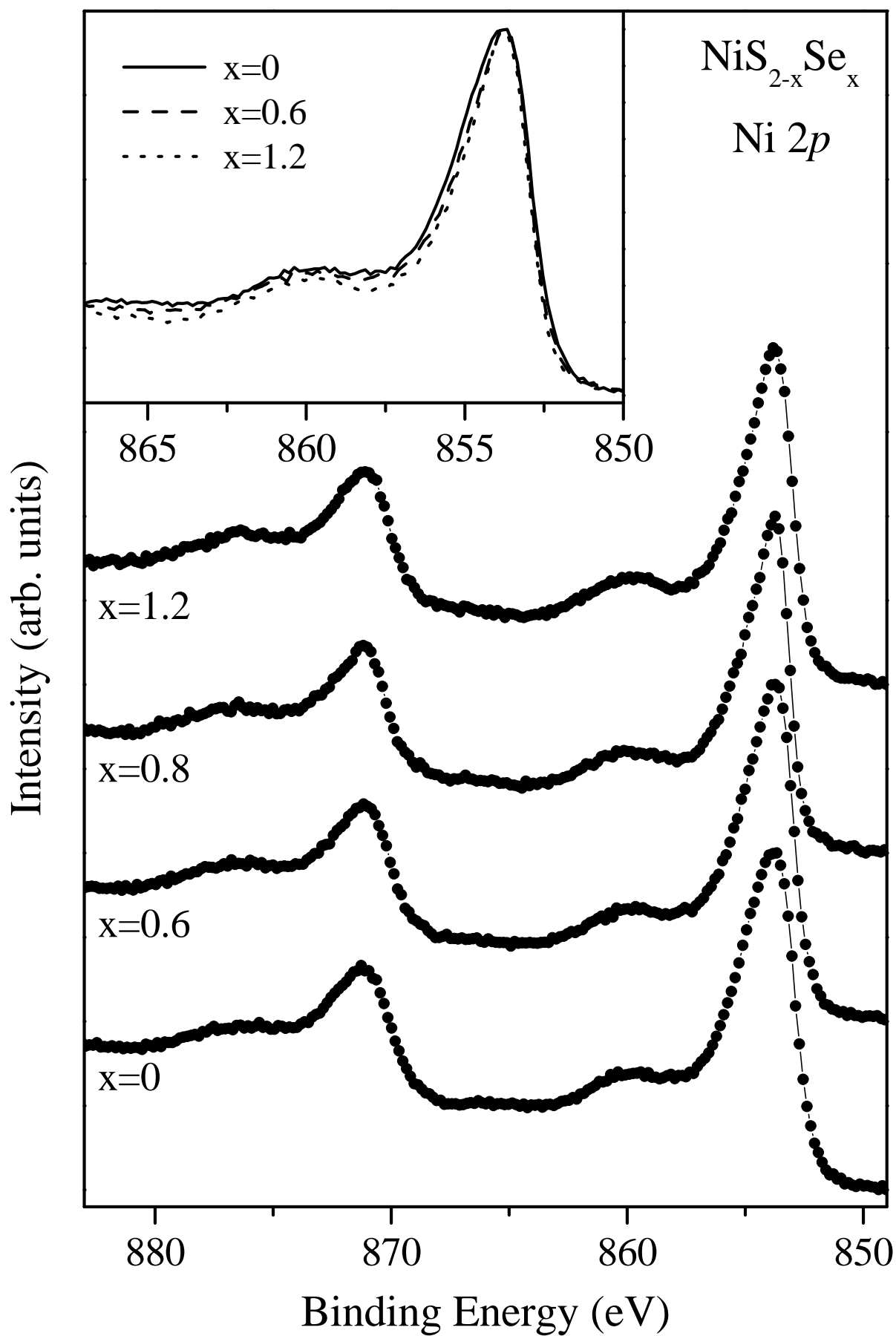
Krishnakumar *et al.*, Fig. 2



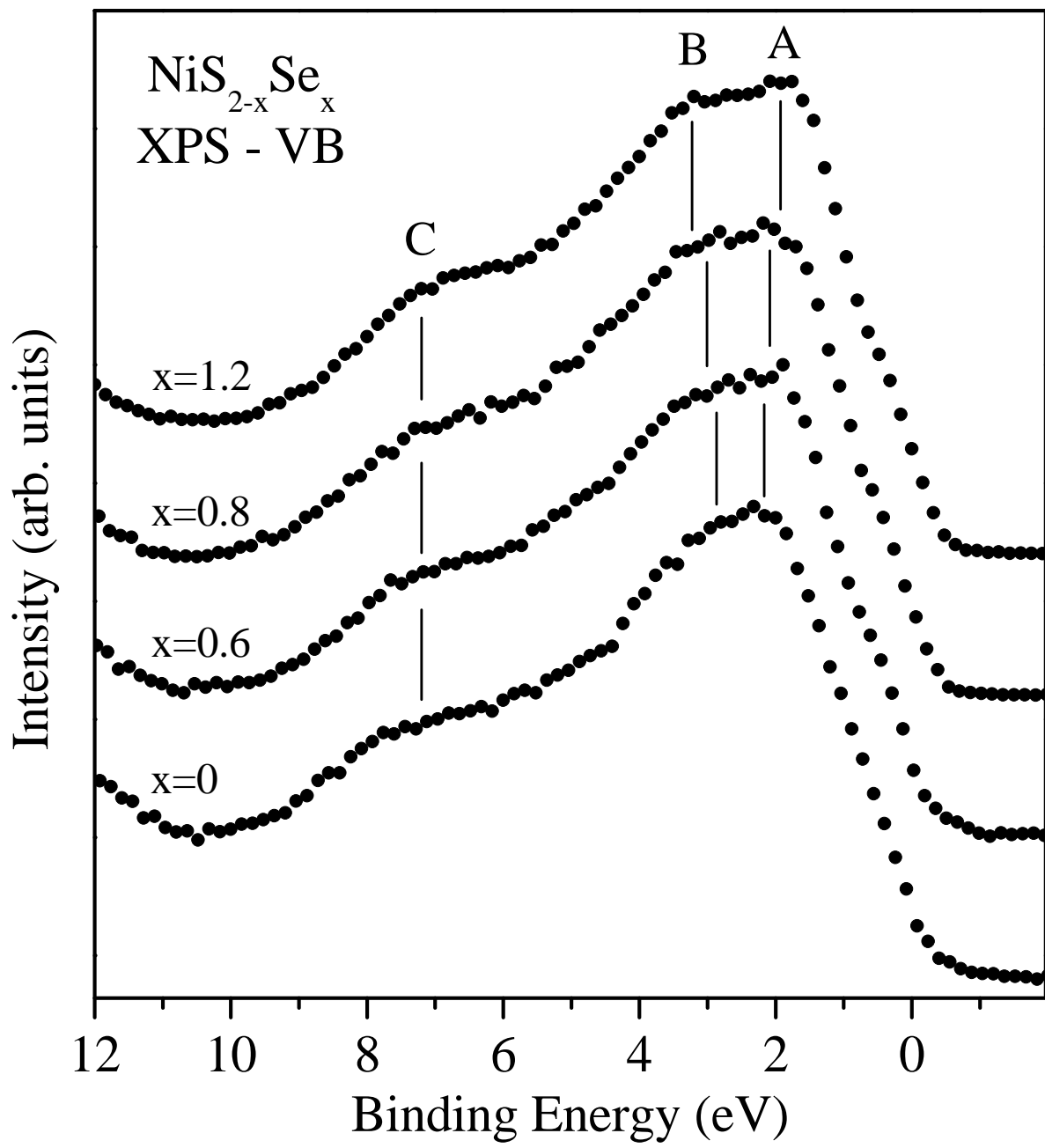
Krishnakumar *et al.*, Fig. 3



Krishnakumar *et al.*, Fig. 4



Krishnakumar *et al.*, Fig. 5



Krishnakumar *et al.*, Fig. 6